Cement and Concrete Research 136 (2020) 106170

Contents lists available at ScienceDirect

Cement and Concrete Research

journal homepage: www.elsevier.com/locate/cemconres

Influences of cross-linking and Al incorporation on the intrinsic mechanical properties of tobermorite

Jiaqi Li[a,*], Wenxin Zhang[a], Krassimir Garbev[b], Günter Beuchle[b], Paulo J.M. Monteiro[a]

[a] Department of Civil and Environmental Engineering, University of California, Berkeley, United States
[b] Institute for Technical Chemistry, Karlsruhe Institute of Technology, 76021 Karlsruhe, Germany

ARTICLE INFO

Keywords:
Tobermorite
C-S-H
Calcium silicate hydrate
High-pressure x-ray diffraction
Intrinsic mechanical properties

ABSTRACT

Tobermorite is the model for calcium aluminosilicate hydrate (C-(A-)S-H), the glue in concrete, and is also the binding phase in cement-based materials under geological conditions and in ancient Roman concrete. Correlating the mechanical properties of tobermorite with atomic structures substantially improves the understanding of C-(A-)S-H. We study this correlation for tobermorite with various Al contents using Raman, nuclear magnetic resonance spectroscopy, and high-pressure X-ray diffraction. Al incorporation shortens the cross-linked tobermorite chains, leading to more charge-balancing Ca and strong H-bonding, and enhancing the incompressibility of the basal-layer of Al-tobermorite. Non-cross-linked tobermorite exhibits high incompressibility of the basal layer but low incompressibility of the interlayer due to lack of cross-linking. The substitution of stronger Si—O with Al—O shows no negative influence on the mechanical properties of tobermorite. The results provide fundamental information on how atomic structure influences the intrinsic properties of C-(A-)S-H and have implications in validating computational methods and parameters.

1. Introduction

Modern concrete, with a history of nearly 200 years, is the second most used materials by mass after water [1]. The binder in modern concrete is ordinary Portland cement (OPC) with the annual production of which exceeds 4 billion tons [2]. Such massive production of OPC contributes to 7% industrial energy consumption and ~9% of anthropogenic CO_2 emission due to the high kilning temperature (i.e., 1450 °C) and process-based CO_2 emission [3]. Substitution of OPC with industrial byproducts (e.g., coal fly ash and ground granulated blast-furnace slag), which are mainly amorphous (calcium) aluminosilicate, is often used to lower the environmental impact of cement/concrete production and to improve the durability performance of cement-based materials [4].

Ancient Roman concrete has been reputable for its structural integrity over 2000 years [5]. The binder in Roman concrete is a mixture of lime and volcanic ash (mainly amorphous aluminosilicate) [6]. The kilning temperature of lime is typically below 900 °C, and the environmental impact of using volcanic ash is minimal [7], allowing Roman concrete production to associate with significantly lower total environmental impacts than modern concrete production. Moreover, the service life of Roman structures is about two orders of magnitude longer than that of modern structures [8]. Thus, it is of great interest to understand the astounding performance of Roman concrete.

Interestingly, modern and ancient concretes share a striking similarity in chemistry. The primary binding phases in Roman concrete are Al-tobermorite and porous calcium (alumino)silicate hydrate C-(A-)S-H, a nanocrystalline phase similar to a defective tobermorite [8] [9] [10] [11]. The primary binding phase in OPC-based modern concrete is also C-(A-)S-H [12] [13], and at curing temperatures > 80 °C (e.g., under steam curing or certain geological conditions) (Al-)tobermorite has also been found in OPC-based materials [14]. In both modern and ancient concretes, C-(A-)S-H and tobermorite are responsible for many physical and mechanical properties [15] [16] [17].

In tobermorite, dreierketten-type silicate tetrahedron chains, which consist of bridging and paired tetrahedra, are flanked on Ca—O sheets to form calcium silicate basal layers [18]. The adjacent basal layers can be either cross-linked by two bridging sites (Fig. 1A) or connected by hydrated Ca (Fig. 1C) [19]. Al incorporation prefers to occur at the bridging site (Fig. 1B) [20]. For C-(A-)S-H, bridging site can be occupied by hydrated Ca, leading to more discrete chains of (alumino)silicate tetrahedra. Experimental and atomistic simulation results in Kumar et al. [10] have proved that this bridging Ca environment is stabilized via a strong hydrogen bonding. Furthermore, C-(A-)S-H typically shows lower structural ordering compared to tobermorite [21] [22] [23].

For structural design, the mechanical properties of concrete are of

* Corresponding author at: University of California, Berkeley, 115 Davis Hall, Berkeley, CA 94720, United States.
E-mail address: Jiaqi.li@berkeley.edu (J. Li).

https://doi.org/10.1016/j.cemconres.2020.106170
Received 19 April 2020; Received in revised form 3 July 2020; Accepted 6 July 2020

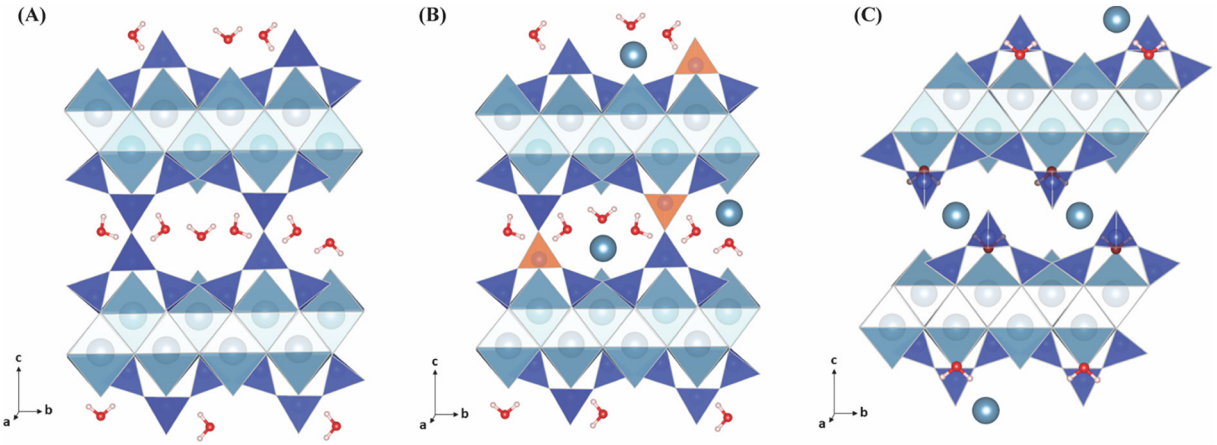

Fig. 1. Schematics of (A) double-chain Al-free 11 Å tobermorite, (B) Al-tobermorite, and (C) single-chain 11 Å tobermorite. The dark blue triangles and orange triangles are silicate tetrahedra and aluminate tetrahedra, respectively. The light-blue diamonds represent Ca—O polyhedra. The blue circles represent interlayer Ca surrounded by water molecules. (For interpretation of the references to color in this figure legend, the reader is referred to the web version of this article.)

great significance. The mechanical properties of porous C-(A-)S-H have been extensively studied at the macro and nano scales [24] [25] [26] [27]. The mechanical properties of C-(A-)S-H at the nano scale have been studied using molecular dynamics [25] and density functional theory (DFT) [28] and have only recently been measured using high-pressure X-ray Raman scattering [29] and high-pressure X-ray diffraction (HP-XRD) [30] [31] [32]. The experimental results showed that the incompressibility of non-cross-linked C-S-H is governed by the densification of its interlayer rather than by the mean silicate chain length [32] [33]. Another HP-XRD study shows that the Al-induced cross-linking sites of aluminosilicate chains act as supporting columns to resist closure of the interlayer under pressure [31]. The influences of Al incorporation and cross-linking sites on the mechanical properties of pore-free C-(A-)S-H have not been decoupled in previous experimental studies. It remains unclear whether it is Al incorporation or the number of cross-linking sites that governs the nanomechanical properties of cross-linked C-(A-)S-H. Moreover, the mechanical properties of tobermorite have only been calculated using DFT [34] [35], the computational results of which have not been rigorously validated by experiments. A recent study coupling Nuclear Magnetic Resonance (NMR) spectroscopy and atomistic simulations [36] have resolved the debates on the nanostructure of C-(A-)S-H and the results have shown higher consistency than previous attempts [25] with recent HP-XRD results of C-(A-)S-H [31] [32]. However, it remains unclear whether it is Al incorporation or cross-linking that governs the mechanical properties of (Al-)tobermorite. Experimental evidences are needed to advance the understanding of the mechanical properties of both C-(A-)S-H and (Al-)tobermorite and to optimize computational methods or parameters (e.g., force fields [37]).

In this study, cross-linked tobermorite (double-chain) with Al/(Al + Si) molar ratio of 0, 1/12, and 1/6 and non-cross-linked tobermorite (single-chain) were synthesized. The influences of Al incorporation and cross-linking on their nanomechanical properties were decoupled in HP-XRD study. ^{29}Si NMR spectroscopy was used to determine the structure of the (alumino)silicate chain in tobermorite. The experimental study provides fundamental information for validating computational studies of tobermorite and tobermorite-like phases (C-(A-)S-H and its derivatives), for understanding the mechanical properties of ancient Roman concrete, and for designing cement-based materials containing (Al-)tobermorite (e.g., steam-cured concrete and oil well cement).

2. Materials and methods

2.1. Materials

11 Å double-chain tobermorite was synthesized as follows: 1) calcium silicate hydrate (C-S-H) slurry with a Ca/Si = 5/6 was mechanochemically produced from CaO (from freshly calcined $CaCO_3$ p.a. at 1000 °C for 2 h), high surface area SiO_2 (Aerosil 200, Evonik), and double distilled water with a H_2O to solid mass ratio of 20. In addition, two C-A-S-H slurries with target Ca/(Si + Al) molar ratios of 5/6, and Al/(Al + Si) molar ratios of 1/12 and 1/6 were prepared by the addition of corresponding quantity of $Al(OH)_3$ (Fluka). All syntheses were performed under nitrogen to avoid sample carbonation. The mechanochemical treatment was performed in an agate ball mill (Pulverisette, Fritsch) for 32 h, according to the method described in [38]. 2) Finally, the resultant slurries were treated hydrothermally in Teflon-lined steel autoclaves at 170 °C for 22 h followed by an additional 2 h at 180 °C. The products were filtered, rinsed with double-distilled, decarbonated water and dried at 60 °C.

14 Å tobermorite was hydrothermally synthesized from a mechanochemically prepared C-S-H phase with a Ca/Si ratio of 5/6 after the procedure described in [39]. The hydrothermal treatment was performed at 70 °C for 12 months. 11 Å single-chain tobermorite was prepared by dehydrating a 14 Å tobermorite at 100 °C for 3 h.

2.2. Methods

2.2.1. ^{29}Si nuclear magnetic resonance

Solid-state ^{29}Si nuclear magnetic resonance (^{29}Si MAS NMR) spectra were taken for the samples on a 59.50 MHz Varian InfinityPlus 300 NMR spectrometer equipped with a 7.1 T widebore Oxford Instruments superconducting magnet and a 6 mm Chemagnetics style MAS probe. A 45° excitation pulse was used, with a recycle delay of 120 s, decoupling at 60 kHz, and MAS at 4.5 kHz. ^{29}Si chemical shifts are given relative to TMS (tetramethylsilane; 0 ppm) using kaolinite as an external standard at −91.2 ppm.

2.2.2. Raman

Raman micro-spectroscopy was performed with a LabRam Aramis (Horiba-Jobin-Yvon) with a spectrograph of focal length: 460 mm equipped with a microscope (Olympus BX41). The excitation wavelength is 473 nm with a power of 11 mW (measured after objective) combined with a grating of 1800 lines/mm. We used a 100× objective (NA = 0.9), and the resulting lateral and vertical resolutions were 0.64 μm and 2.3 μm, respectively. Single spots were measured with an

exposition of 5 s and 64 accumulations.

2.2.3. HP-XRD

The HP-XRD experiment was conducted at beamline 12.2.2 of the Advanced Light Source at the Lawrence Berkeley National Laboratory. A BX-90 diamond anvil cell with an axial geometry set-up was used. The diameter of the diamond culet was ~400 μm. Stainless steel gaskets were prepared with a cylindrical chamber of ~100 μm in thickness and ~120 μm in diameter. A ruby sphere (α-Al_2O_3 doped with 0.05 wt.% Cr^{3+}) was loaded with each tobermorite sample into the chamber. Then, the chamber was filled with methanol-ethanol solution (4:1 by volume) as a pressure medium. The ruby spheres were used as a pressure gage to measure the hydrostatic pressure in the chamber using the ruby florescence calibration method. The incident X-ray beam energy was 25 keV with beam size of ~30 μm. The sample-to-detector (MAR345 image plate) distance was ~330 mm. Lattice constants were refined using *CelRef*, with Merlino's tobermorite structure of B11m space group [18]. See Supplementary information for more details.

3. Results and discussions

Fig. 2 shows the ^{29}Si NMR spectra of the double-chain 11 Å (Al-) tobermorite. The Al-free double-chain tobermorite is highly polymerized as the fraction of end-of chain silica (Q^1) at ~ − 80 ppm [40] is significantly low (see Table 1 for fractions). Al incorporation give rise to alumina cross-linking site (evidenced by increased Q^3(1Al) fraction) at the expense of silicate cross-linking (Q^3(0Al)) [41]. As the Al content increases, Al-tobermorite shows a lower degree of polymerization with more Q^1 and a comparable number of cross-linked sites (Q^3(0Al) and Q^3(1Al)). The mean silicate chain lengths of the double-chain tobermorite with Al/(Al + Si) of 0, 1/12, and 1/6 are 135, 73, and 28, respectively.

Fig. 3 shows the Raman spectra of Al-free double chain 11 Å tobermorite (A), single chain 11 Å (B) and fully substituted Al-tobermorite (Al/(Al + Si) =1/6) (C). The main feature in all three spectra is the Si-O-Si bending vibration in Q_2 chains [39] [42] which frequency varies from 682 cm^{-1} (double chains) to 680 cm^{-1} (single chains) and finally to 669 cm^{-1} in Al substituted tobermorite. Double chain 11 Å tobermorite shows an additional band at 620 cm^{-1} which is characteristic for Q_3 sites [42] [43]. The Raman spectrum in Fig. 3B lacks this band clearly showing an absence of cross-linking sites in the single-chain 11 Å tobermorite. Similar results were obtained by Biagioni et al. in Raman spectra after thermal treatment of plombierite

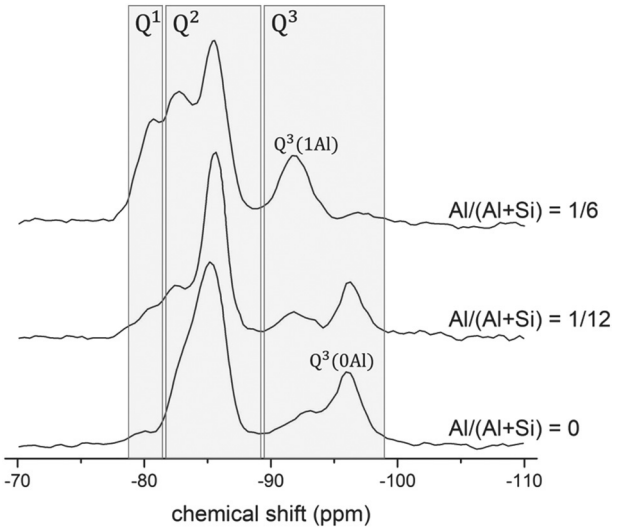

Fig. 2. ^{29}Si NMR spectra of double-chain 11 Å tobermorite with various Al contents.

(14 Å tobermorite) [44]. In addition to the band shifts to lower frequencies, there is a substantial broadening of the Raman signals witnessing increasing structural disorder upon thermal treatment. In the Raman spectrum of Al substituted 11 Å tobermorite (Al/(Al + Si) = 1/6) the band at 620 cm^{-1} is also not observed, confirming the absence of Si-O-Si linkages of type Q_3. Instead a band at 568 cm^{-1} appears belonging to Al-O-Si vibrational modes according to the Loewenstein rule. Another interesting feature is the presence of a band at 949 cm^{-1} which can be attributed to Si-OH stretching vibrations thus confirming the substitution $Si^{4+} \rightarrow Al^{3+} + H^{1+}$ in Al-tobermorite.

The unit cell parameters of tobermorite with various Al contents and with/without cross-linking at ambient pressure do not show significant variations (Table 2). As applied hydrostatic pressure increases, the diffraction peaks of tobermorite monotonically shift to the right (Fig. 3), suggesting a systematic decrease of interplanar distances (e.g., a closing interlayer spacing indicated by the shift in (002) peaks). Pressure-induced broadening is observed for all peak at elevated pressure due to amorphization (i.e., reduction in structural ordering) of the sample caused by compression [45]. This pressure-induced amorphization is commonly observed in HP-XRD studies, including studies of phases in cementitious materials [46] [47] [48] [49].

The incompressibility of the unit cell along a-, b-, and c-axes is defined with the Biot strain along each axis as a function of applied hydrostatic pressure. The incompressibility along a- and b-axes (Fig. 4A) of all double-chain tobermorite lies within −1/245 and −1/280 GPa^{-1}, highly comparable to previously reported results of cross-linked C-A-S-H [31]. The ab-planar stiffness (negative inverse of the incompressibility) of double-chain tobermorite systematically increases with increased Al/(Al + Si). With Al substitution, tobermorite bears a greater number of charge-balancing Ca atom in the interlayer and/or stronger H-bonding [20]. These extra Ca atoms and stronger H-bonding enhance the steric constraints of the ab-plane (calcium silicate basal layer), resulting in the stiffer ab-plane in Al-tobermorite. The incompressibility of single-chain tobermorite along a- and b-axes are −1/293 and −1/322 GPa^{-1}, respectively, comparable to previous results of Al-free non-cross-linked C-(A-)S-H [32,33]. The ab-plane of single-chain tobermorite is slightly stiffer than that of double-chain tobermorite, due to more charge-balancing Ca in the interlayer and a stronger H-bond system of single-chain tobermorite (i.e., more steric constraints). Cross-linking does not stiffen the ab-plane of tobermorite, as explained by a hinge deformation mechanism [34]: the shared oxygen atom of the cross-linking sites acts as a hinge, and the entire set of atoms (i.e., Si and Al) which bond to the shared O atom pivots around the hinge. Instead of contraction of covalent bonds (Si-O-Si and/or Si-O-Al) at the cross-linking sites across the interlayer, reorientation of the bonds requires less energy. The stiffening of ab-plane by cross-linking is not observed in cross-linked C-(A-)S-H [31].

Biot strain along c-axis versus hydrostatic pressure of all tobermorite samples can be fitted with a linear trendline in Fig. 5B. The incompressibility of cross-linked tobermorite lies within a narrow range between −1/225 and −1/250 GPa^{-1}, suggesting that the influence of Al substitution on the c-axis incompressibility is insignificant. Although AlO_4 occupies many cross-linking sites and its Al—O bond is typically longer than Si—O (1.75 Å in AlO_4 versus 1.62 Å in SiO_4) [50], the Al-tobermorite with higher Al content is not softer than Al-free cross-linked 11 Å tobermorite, indicating that reorientation, rather than simply contraction of Si—O or Al—O bonds, around cross-linking sites governs the c-axis stiffness. Otherwise, the longer Al—O bond in AlO_4 relative to Si—O in SiO_4 would contribute to lower c-axis incompressibility of Al-tobermorite. The incompressibility of single-chain 11 Å tobermorite along c-axis is −1/150 GPa^{-1}, lower than those of double-chain tobermorite. The lower stiffness of single-chain tobermorite is explained by the absence of cross-linking sites, which resist the closure of interlayer space under compression [34]. The interlayer Ca in single-chain tobermorite shields the Coulomb interaction across the interlayer, leading to a softer interlayer space [34]. Thus, it can be

Table 1
Measured fraction of Si environments in double-chain 11 Å tobermorite from NMR and calculated mean (alumino) silicate chain length (MCL).

Al/(Al + Si)	Q^1	Q^2(1Al)	Q^2(0Al)	Q^3(1Al)/ Q^3 (extra)*	Q^3(0Al)	Cross-linking site	MCL
0	0.03	0	0.63	0.14	0.21	0.33	135
1/12	0.06	0.11	0.55	0.09	0.19	0.32	73
1/6	0.17	0.23	0.36	0.21	0.03	0.33	28

*Q^3(extra) is assigned to cross-linked Q^3 charge-balanced by Ca.

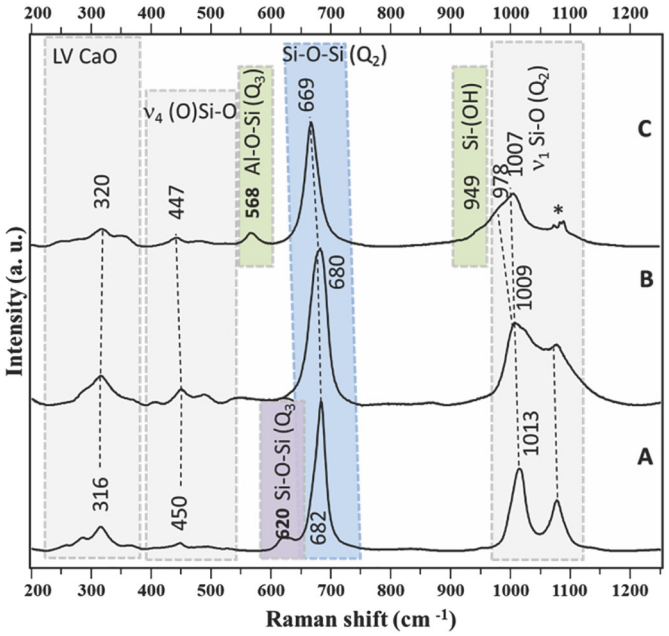

Fig. 3. Raman spectra in the range of 200–1250 cm^{-1} of Al-free double chain tobermorite. A) Al-free single chain tobermorite; B) and fully substituted Al tobermorite (Al/(Al + Si) = 1/6). The asterisk denotes CO_3 bands of a vaterite impurity.

Table 2
Measured cell parameters of 11 Å tobermorite at ambient pressure.

	Al/(Al + Si)	a (Å)	b (Å)	c (Å)	γ (°)
Single chain	0	6.719	7.342	23.50	123.12
Double chain	0	6.734	7.370	22.71	123.17
	1/12	6.725	7.386	22.86	123.31
	1/6	6.722	7.397	23.21	123.38

concluded that cross-linking sites enhance the stiffness along c-axis. Geng et al. studied the nanomechanical properties of C-(A-)S-H synthesized at 80 °C using HP-XRD [31], in which the stiffening along c-axis by aluminate cross-linking sites is also found.

The measured K_0 of single-chain tobermorite is 57 ± 2 GPa (Fig. 5C), which is consistent with DFT-simulated K_0 of 58 GPa [34]. The measured K_0 of Al-free double-chain tobermorite is 63 ± 3 GPa, also consistent with K_0 of 67–68 GPa in the DFT study [34] [35], but does not agree with another DFT study [51], where the calculated K_0 of Al-free double-chain tobermorite is 77 GPa. The measured K_0 of single-chain tobermorite is lower mainly due to the absence of cross-linking sites. Our previous HP-XRD study of C-(A-)S-H synthesized at 80 °C also shows lower K_0 (~21 GPa lower) for C-S-H in the absence of cross-linking sites relative to that with cross-linking sites [31]. The double-chain Al-tobermorite exhibits 7–8 GPa higher measured K_0 than Al-free double-chain tobermorite. The measured K_0 of synthetic Al-tobermorite in this study, 63 ± 3 GPa, is slightly higher than that of Al-tobermorite found in ancient Roman concrete (55 ± 5 GPa) [16]. We assign the lower K_0 of Al-tobermorite in ancient Roman concrete to the structural distortion caused by potassium incorporation in the interlayer [28] [5]. Al substitution slightly stiffens the tobermorite due to stiffening in the ab-plane through a greater number of charge-balancing Ca or stronger H-bonding alternatively. Another possibility that has been evidenced in a C-(A-)S-H study [10] may also explain the positive correlation between the Al content and mechanical properties of cross-linked tobermorite—the Al-induced shorter aluminosilicate chains can accommodate more bridging Ca and thus a strong hydrogen bonding system can form. Although the number of bridging Ca of (Al-)tobermorite is lower than that of C-(A-)S-H at high Ca/Si ratios [10], the possible influences of bridging Ca and strong hydrogen bonding here should not be ruled out. Indeed, the Raman spectrum of Al-tobermorite in Fig. 3C shows presence of additional OH groups which must be involved in strong H-bonding system in the ab-plane supported by shortening of the b-axis. Despite the positive correlation between mean silicate chain length and mechanical properties of C-S-H [27], we do not observe a positive correlation between mean aluminosilicate chain length and the mechanical properties of tobermorite. Instead, a negative trend between chain length and mechanical properties of tobermorite is found.

4. Conclusions

The present study systematically investigates the correlation between the structure and the intrinsic mechanical properties of 11 Å tobermorite and Al-tobermorite using NMR and HP-XRD. The influences of Al substitution and cross-linking sites on the mechanical properties of 11 Å tobermorite are studied. Experimental results show that Al incorporation shortens the aluminosilicate chain length of tobermorite. The incompressibility of cross-linked tobermorite along the a- and b-axes increases with Al substitution due to an increased number of charge-balancing Ca, which enhances the steric constraints in the ab-plane. Alternatively, if balanced by $Al^{3+} + H^+ \rightarrow Si^{4+}$ as shown by Raman data, the additional OH groups would be involved in a fairly strong H-bond system (favored by shorter b-axis), which also contributes to stiffening of the ab-plane. Similarly, the ab-planar incompressibility of non-cross-linked tobermorite is higher than that of cross-linked tobermorite since the lack of cross-linking sites also leads to presence either of more interlayer Ca, or stronger H-bonding for steric constraints. Cross-linking sites act as supporting columns to stiffen the interlayer space along the c-axis but do not stiffen the tobermorite in the ab-plane. Both Al substitution and cross-linking sites increase the bulk modulus of tobermorite, and Al-tobermorite exhibits the highest bulk modulus while single-chain tobermorite shows the lowest bulk modulus. An inverse correlation between the mechanical properties of cross-linked tobermorite and its aluminosilicate chain length is found. The experimental results in the present work have great implications for validating the use of different computational methods, different force fields (e.g., CSH-FF, cement-FF, and Clay-FF) and associated parameters (e.g., Lennard-Jones pair coefficient) in the study of PC-based materials, particularly in the study of mechanical behaviors of C-(A-)S-H and tobermorite. Specifically, the strong H-bond system in Al-tobermorite and the interaction between the H-bond and bridging Ca of short aluminosilicate chains could be examined in computational studies at the atomistic-level. Additionally, the influences of charge-balancing ions on the nanomechanical properties of (Al-)tobermorite could also be examined in computational studies. The measured

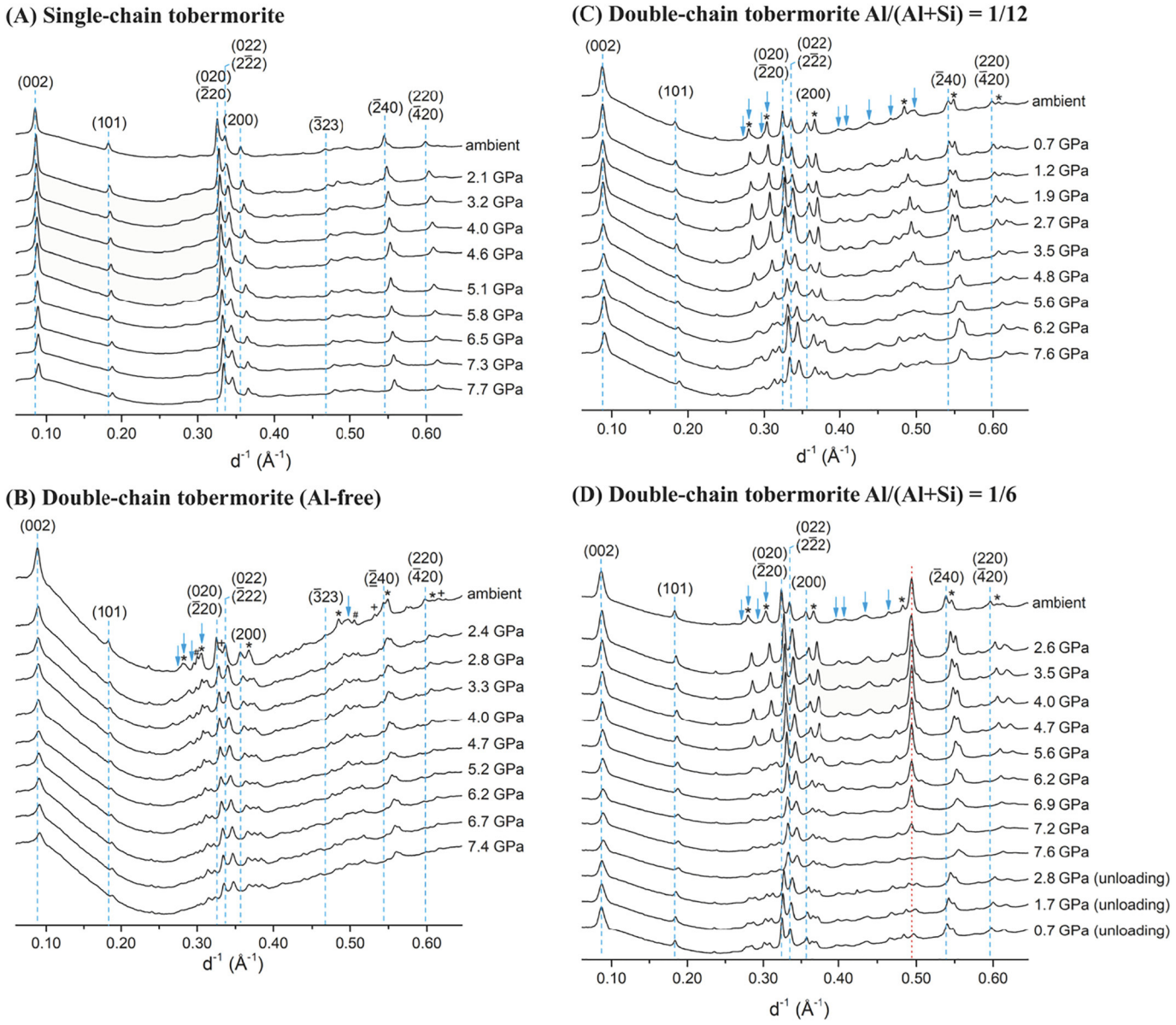

Fig. 4. X-ray diffractogram of A) single-chain Al-free 11 Å tobermorite, B) double-chain Al-free tobermorite, C) double-chain tobermorite (Al/(Al + Si) =1/12), D) double-chain tobermorite (Al/(Al + Si) =1/6) as a function of applied hydrostatic pressure. The tobermorite peaks, which were not used for refinement, are indicated with blue arrows. The impurities are labeled with asterisk (vaterite), cross (calcite), and pound sign (aragonite). The red dot line indicates the diffraction from the gasket. (For interpretation of the references to color in this figure legend, the reader is referred to the web version of this article.)

intrinsic mechanical properties of different tobermorites in this study could be implemented for design of sustainable and high-performance concrete using bottom-up approaches.

CRediT authorship contribution statement

Jiaqi Li:Conceptualization, Methodology, Investigation, Validation, Visualization, Writing - original draft.**Wenxin Zhang**:Investigation, Visualization, Writing - review & editing.**Krassimir Garbev**:Investigation, Methodology, Visualization, Writing - original draft.**Günter Beuchle**:Investigation, Methodology, Visualization, Writing - original draft.**Paulo J.M. Monteiro**:Writing - review & editing, Supervision, Funding acquisition.

Declaration of competing interest

The authors declare that they have no known competing financial interests or personal relationships that could have appeared to influence the work reported in this paper.

Acknowledgment

This work is funded by the US National Science Foundation under the SusChEM Program, grant # DMR-1410557 and Division of Materials Research Ceramics Program, DMR-CER, grant # 1935604. The Advanced Light Source is supported by the Director, Office of Science, Office of Basic Energy Sciences, of the U.S. Department of Energy under contract no. DE-AC02-05CH11231. We thank the support from Dr. Jinyuan Yan at the Advanced Light Source. David Gardner at UC Berkeley is thanked for the assistance of the HP-XRD experiment.

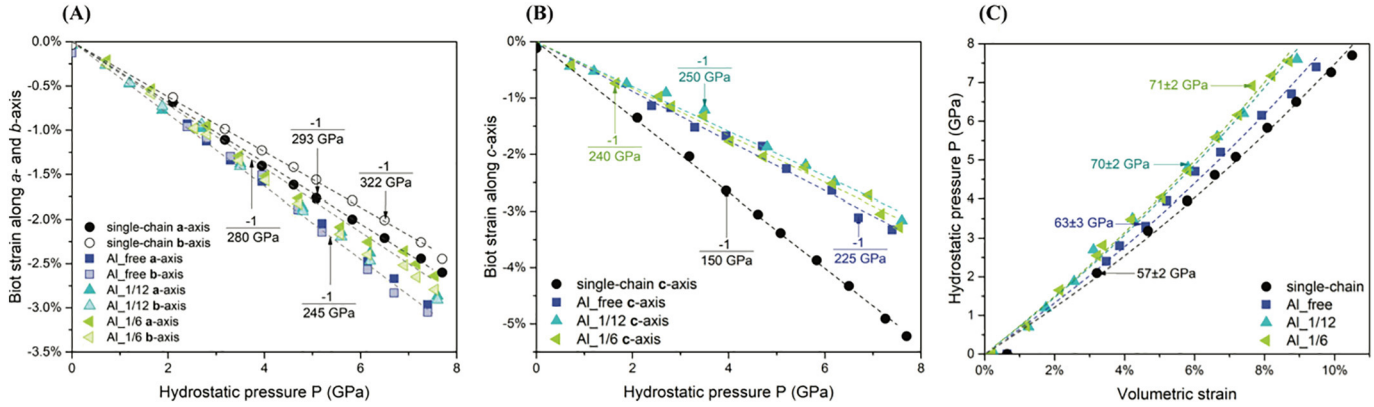

Fig. 5. Strain as a function of applied hydrostatic pressure along A) Biot strain along a- and b-axes; B) Biot strain along c-axis; C) Volumetric strain. The slope of each dash line represents the incompressibility along the axis, equal to the negative inverse of the stiffness along the axis. The uncertainty of pressure is estimated to be 0.1 GPa. The uncertainty of the Biot stain is below ~0.2%. R^2 of all fittings in C) are above 0.99.

Appendix A. Supplementary data

Supplementary data to this article can be found online at https://doi.org/10.1016/j.cemconres.2020.106170.

References

[1] R.J. Myers, G.Q. Geng, J.Q. Li, E.D. Rodriguez, J.Y. Ha, P. Kidkhunthod, G. Sposito, L.N. Lammers, A.P. Kirchheim, P.J.M. Monteiro, Role of adsorption phenomena in cubic tricalcium aluminate dissolution, Langmuir 33 (2017) 45–55.

[2] P.J.M. Monteiro, S.A. Miller, A. Horvath, Towards sustainable concrete, Nat. Mater. 16 (2017) 698–699.

[3] M.C.G. Juenger, R. Snellings, S.A. Bernal, Supplementary cementitious materials: new sources, characterization, and performance insights, Cement Concrete Res 122 (2019) 257–273.

[4] I. Diaz-Loya, M. Juenger, S. Seraj, R. Minkara, Extending supplementary cementitious material resources: reclaimed and remediated fly ash and natural pozzolans, Cement Concrete Comp 101 (2019) 44–51.

[5] M.D. Jackson, S.R. Chae, S.R. Mulcahy, C. Meral, R. Taylor, P. Li, A.-H. Emwas, J. Moon, S. Yoon, G. Vola, Unlocking the secrets of Al-tobermorite in Roman seawater concrete, Am. Mineral. 98 (2013) 1669–1687.

[6] M.D. Jackson, E.N. Landis, P.F. Brune, M. Vitti, H. Chen, Q.F. Li, M. Kunz, H.R. Wenk, P.J.M. Monteiro, A.R. Ingraffea, Mechanical resilience and cementitious processes in Imperial Roman architectural mortar, P Natl Acad Sci USA 111 (2014) 18484–18489.

[7] S.A. Miller, R.J. Myers, Environmental impacts of alternative cement binders, Environ Sci Technol 54 (2020) 677–686.

[8] A. Palomo, P. Monteiro, P. Martauz, V. Bilek, A. Fernandez-Jimenez, Hybrid binders: a journey from the past to a sustainable future (opus caementicium futurum), Cem. Concr. Res. 124 (2019) 105829.

[9] I.G. Richardson, Model structures for C-(A)-SH (I), Acta Crystallogr. Sect. B: Struct. Sci. Cryst. Eng. Mater. 70 (2014) 903–923.

[10] A. Kumar, B.J. Walder, A.K. Mohamed, A. Hofstetter, B. Srinivasan, A.J. Rossini, K. Scrivener, L. Emsley, P. Bowen, The atomic-level structure of cementitious calcium silicate hydrate, J. Phys. Chem. C 121 (2017) 17188–17196.

[11] S. Merlino, E. Bonaccorsi, T. Armbruster, The real structure of tobermorite 11 angstrom: normal and anomalous forms, OD character and polytypic modifications, Eur. J. Mineral. 13 (2001) 577–590.

[12] E. L'Hopital, B. Lothenbach, D.A. Kulik, K. Scrivener, Influence of calcium to silica ratio on aluminium uptake in calcium silicate hydrate, Cement Concrete Res 85 (2016) 111–121.

[13] J. Li, G. Geng, R. Myers, Y.S. Yu, D. Shapiro, C. Carraro, R. Maboudian, P.J.M. Monteiro, The chemistry and structure of calcium (alumino) silicate hydrate: a study by XANES, ptychographic imaging, and wide- and small-angle scattering, Cem. Concr. Res. 115 (2019) 367–378.

[14] G.L. Kalousek, A.F. Prebus, Crystal chemistry of hydrous calcium silicates. 3. Morphology and other properties of Tobermorite and related phases, J. Am. Ceram. Soc. 41 (1958) 124–132.

[15] P.K. Mehta, P.J. Monteiro, Concrete Microstructure, Properties and Materials, (2017).

[16] M.D. Jackson, J. Moon, E. Gotti, R. Taylor, S.R. Chae, M. Kunz, A.H. Emwas, C. Meral, P. Guttmann, P. Levitz, H.R. Wenk, P.J.M. Monteiro, Material and elastic properties of Al-Tobermorite in ancient Roman seawater concrete, J. Am. Ceram. Soc. 96 (2013) 2598–2606.

[17] P.J.M. Monteiro, G.Q. Geng, D. Marchon, J.Q. Li, P. Alapati, K.E. Kurtis, M.J.A. Qomi, Advances in characterizing and understanding the microstructure of cementitious materials, Cem. Concr. Res. 124 (2019) 105806.

[18] S. Merlino, E. Bonaccorsi, M. Merlini, F. Marchetti, W. Garra, Tobermorite 11 angstrom and its synthetic counterparts: structural relationships and thermal behaviour, Minerals as Advanced Materials I (2008) 37–44.

[19] S. Hamid, The crystal structure of the 11 Ä natural tobermorite Ca2. 25 [Si3O7. 5 (OH) 1.5]·1H2O, Zeitschrift für Kristallographie-Crystalline Materials 154 (1981) 189–198.

[20] C. Biagioni, S. Merlino, E. Bonaccorsi, The tobermorite supergroup: a new nomenclature, Mineral. Mag. 79 (2015) 485–495.

[21] J. Li, G. Geng, W. Zhang, Y.S. Yu, D.A. Shapiro, P.J.M. Monteiro, The hydration of beta- and alpha(H)'-Dicalcium silicates: an X-ray spectromicroscopic study, ACS Sustain. Chem. Eng. 7 (2019) 2316–2326.

[22] L.B. Skinner, S.R. Chae, C.J. Benmore, H.R. Wenk, P.J.M. Monteiro, Nanostructure of calcium silicate hydrates in cements, Phys. Rev. Lett. 104 (2010) 195502.

[23] C.E. White, L.L. Daemen, M. Hartl, K. Page, Intrinsic differences in atomic ordering of calcium (alumino)silicate hydrates in conventional and alkali-activated cements, Cement Concrete Res 67 (2015) 66–73.

[24] F.J. Ulm, M. Vandamme, H.M. Jennings, J. Vanzo, M. Bentivegna, K.J. Krakowiak, G. Constantinides, C.P. Bobko, K.J. Van Vliet, Does microstructure matter for statistical nanoindentation techniques? Cement Concrete Comp 32 (2010) 92–99.

[25] M.J.A. Qomi, K.J. Krakowiak, M. Bauchy, K.L. Stewart, R. Shahsavari, D. Jagannathan, D.B. Brommer, A. Baronnet, M.J. Buehler, S. Yip, F.J. Ulm, K.J. Van Vliet, R.J.M. Pellenq, Combinatorial molecular optimization of cement hydrates, Nat. Commun. 5 (2014) 1–10.

[26] R. Hay, J. Li, K. Celik, Influencing factors on micromechanical properties of calcium (alumino) silicate hydrate C-(A-) SH under nanoindentation experiment, Cem. Concr. Res. 134 (2020) 106088.

[27] W. Kunther, S. Ferreiro, J. Skibsted, Influence of the Ca/Si ratio on the compressive strength of cementitious calcium-silicate-hydrate binders, J. Mater. Chem. A 5 (2017) 17401–17412.

[28] V.O. Ozcelik, C.E. White, Nanoscale charge-balancing mechanism in alkali-substituted calcium-silicate-hydrate gels, J. Phys. Chem. Lett. 7 (2016) 5266–5272.

[29] J. Li, W. Zhang, P.J. Monteiro, Synchrotron X-ray Raman scattering shows the changes of the Ca environment in CSH exposed to high pressure, Cem. Concr. Res. 132 (2020) 106066.

[30] G. Geng, R.N. Vasin, J. Li, M.J.A. Qomi, J. Yan, H.R. Wenk, P.J.M. Monteiro, Preferred orientation of calcium aluminosilicate hydrate induced by confined compression, Cem. Concr. Res. 113 (2018) 186–196.

[31] G. Geng, R.J. Myers, J. Li, R. Maboudian, C. Carraro, D.A. Shapiro, P.J. Monteiro, Aluminum-induced dreierketten chain cross-links increase the mechanical properties of nanocrystalline calcium aluminosilicate hydrate, Sci. Rep. 7 (2017) 44032.

[32] G. Geng, R.J. Myers, M.J.A. Qomi, P.J.M. Monteiro, Densification of the interlayer spacing governs the nanomechanical properties of calcium-silicate-hydrate, Sci. Rep. 7 (2017) 10986.

[33] J. Li, W. Zhang, P.J.M. Monteiro, The structure and intrinsic mechanical properties of nanocrystalline calcium silicate hydrate, ACS Sustain. Chem. Eng., (Submitted).

[34] R. Shahsavari, M.J. Buehler, R.J.M. Pellenq, F.J. Ulm, First-principles study of elastic constants and interlayer interactions of complex hydrated oxides: case study of Tobermorite and Jennite, J. Am. Ceram. Soc. 92 (2009) 2323–2330.

[35] C. Dharmawardhana, M. Bakare, A. Misra, W.Y. Ching, Nature of interatomic bonding in controlling the mechanical properties of calcium silicate hydrates, J. Am. Ceram. Soc. 99 (2016) 2120–2130.

[36] A. Kunhi Mohamed, P. Moutzouri, P. Berruyer, B.J. Walder, J. Siramanont, M. Harris, M. Negroni, S.C. Galmarini, S.C. Parker, K.L. Scrivener, L. Emsley, P. Bowen, The atomic-level structure of cementitious calcium aluminate silicate hydrate, J. Am. Chem. Soc. 142 (2020) 11060–11071.

[37] R.K. Mishra, A.K. Mohamed, D. Geissbuhler, H. Manzano, T. Jamil, R. Shahsavari, A.G. Kalinichev, S. Galmarini, L. Tao, H. Heinz, R. Pellenq, A.C.T. van Duin, S.C. Parker, R.J. Flatt, P. Bowen, Cemff: a force field database for cementitious materials including validations, applications and opportunities, Cement Concrete Res 102 (2017) 68–89.

[38] L. Black, A. Stumm, K. Garbev, P. Stemmermann, K.R. Hallam, G.C. Allen, X-ray photoelectron spectroscopy of aluminium-substituted tobermorite, Cement Concrete Res 35 (2005) 51–55.

[39] K. Garbev, P. Stemmermann, L. Black, C. Breen, J. Yarwood, B. Gasharova, Structural features of C-S-H(I) and its carbonation in air - a Raman spectroscopic study. Part I: fresh phases, J. Am. Ceram. Soc. 90 (2007) 900–907.
[40] B. Lothenbach, D. Nied, E. L'Hopital, G. Achiedo, A. Dauzeres, Magnesium and calcium silicate hydrates, Cement Concrete Res 77 (2015) 60–68.
[41] R.J. Myers, E. L'Hopital, J.L. Provis, B. Lothenbach, Effect of temperature and aluminium on calcium (alumino)silicate hydrate chemistry under equilibrium conditions, Cement Concrete Res 68 (2015) 83–93.
[42] R.J. Kirkpatrick, J.L. Yarger, P.F. McMillan, P. Yu, X.D. Cong, Raman spectroscopy of C-S-H, tobermorite, and jennite, Adv. Cem. Based Mater. 5 (1997) 93–99.
[43] C. Biagioni, E. Bonaccorsi, M. Lezzerini, M. Merlini, S. Merlino, Thermal behaviour of tobermorite from N'Chwaning II mine (Kalahari manganese field, Republic of South Africa). I. Thermo-gravimetric and X-ray diffraction studies, Eur. J. Mineral. 24 (2012) 981–989.
[44] C. Biagioni, E. Bonaccorsi, S. Merlino, D. Bersani, New data on the thermal behavior of 14 angstrom tobermorite, Cement Concrete Res 49 (2013) 48–54.
[45] G.Q. Geng, J.Q. Li, Y. Zhou, L. Liu, J.Y. Yan, M. Kunz, P.J.M. Monteiro, A high-pressure X-ray diffraction study of the crystalline phases in calcium aluminate cement paste, Cement Concrete Res 108 (2018) 38–45.
[46] J. Moon, S. Yoon, P.J.M. Monteiro, Mechanical properties of jennite: a theoretical and experimental study, Cem. Concr. Res. 71 (2015) 106–114.
[47] J.H. Moon, J.E. Oh, M. Balonis, F.P. Glasser, S.M. Clark, P.J.M. Monteiro, Pressure induced reactions amongst calcium aluminate hydrate phases, Cement Concrete Res 41 (2011) 571–578.
[48] J. Moon, J.E. Oh, M. Balonis, F.P. Glasser, S.M. Clark, P.J.M. Monteiro, High pressure study of low compressibility tetracalcium aluminum carbonate hydrates 3CaO center dot Al2O3 center dot CaCO3 center dot 11H(2)O, Cem. Concr. Res. 42 (2012) 105–110.
[49] J. Li, W. Zhang, P.J.M. Monteiro, Mechanical properties of struvite-K: a high-pressure X-ray diffraction study, Cem. Concr. Res., (Submitted).
[50] D. Liang, Z.M. Yan, X.W. Lv, J. Zhang, C.G. Bai, Transition of blast furnace slag from silicate-based to aluminate-based: structure evolution by molecular dynamics simulation and Raman spectroscopy, Metall. Mater. Trans. B Process Metall. Mater. Process. Sci. 48 (2017) 573–581.
[51] C.C. Dharmawardhana, A. Misra, S. Aryal, P. Rulis, W.Y. Ching, Role of interatomic bonding in the mechanical anisotropy and interlayer cohesion of CSH crystals, Cem. Concr. Res. 52 (2013) 123–130.